The Astrophysical Journal, 703:1890–1903, 2009 October 1 doi:10.1088/0004-637X/703/2/1890
© 2009. The American Astronomical Society. All rights reserved. Printed in the U.S.A.

A VIRTUAL SKY WITH EXTRAGALACTIC H I AND CO LINES FOR THE SQUARE KILOMETRE ARRAY AND THE ATACAMA LARGE MILLIMETER/SUBMILLIMETER ARRAY*

D. Obreschkow[1], H.-R. Klöckner[1], I. Heywood[1], F. Levrier[2], and S. Rawlings[1]
[1] Astrophysics, Department of Physics, University of Oxford, Keble Road, Oxford, OX1 3RH, UK
[2] Ecole Normale Supérieure, LERMA-LRA, UMR 8112 du CNRS, 24 rue Lhomond 75231, Paris Cedex 05, France
Received 2009 April 16; accepted 2009 August 12; published 2009 September 15

ABSTRACT

We present a sky simulation of the atomic H I-emission line and the first 10 $^{12}C^{16}O$ rotational emission lines of molecular gas in galaxies beyond the Milky Way. The simulated sky field has a comoving diameter of $500\,h^{-1}$ Mpc; hence, the actual field of view depends on the (user-defined) maximal redshift z_{max}; e.g., for $z_{max} = 10$, the field of view yields $\sim 4 \times 4$ deg^2. For all galaxies, we estimate the line fluxes, line profiles, and angular sizes of the H I and CO-emission lines. The galaxy sample is complete for galaxies with cold hydrogen masses above $10^8\,M_\odot$. This sky simulation builds on a semi-analytic model of the cosmic evolution of galaxies in a Λ cold dark matter (ΛCDM) cosmology. The evolving CDM distribution was adopted from the Millennium Simulation, an *N*-body CDM simulation in a cubic box with a side length of $500\,h^{-1}$ Mpc. This side length limits the coherence scale of our sky simulation: it is long enough to allow the extraction of the baryon acoustic oscillations in the galaxy power spectrum, yet the position and amplitude of the first acoustic peak will be imperfectly defined. This sky simulation is a tangible aid to the design and operation of future telescopes, such as the Square Kilometre Array, Large Millimeter Telescope, and Atacama Large Millimeter/Submillimeter Array. The results presented in this paper have been restricted to a graphical representation of the simulated sky and fundamental dN/dz analyses for peak flux density limited and total flux limited surveys of H I and CO. A key prediction is that H I will be harder to detect at redshifts $z \gtrsim 2$ than predicted by a no-evolution model. The future verification or falsification of this prediction will allow us to qualify the semi-analytic models.

Key words: cosmology: theory – galaxies: evolution – galaxies: high-redshift – ISM: atoms – ISM: molecules

Online-only material: color figures

1. INTRODUCTION

The interstellar medium (ISM) is the bridge between the environment of galaxies and their newborn stars. Its atomic and molecular phases can be detected via emission lines. Typically studied lines include the H I-radio line (1.420 GHz rest frame) and the rotational CO lines in the (sub)millimeter spectrum (multiples of 115.27 GHz). These lines characterize both the composition and the dynamical state of the ISM, and their apparent frequency measures the redshift of the source. If the object sits at a cosmological distance, the redshift is dominated by the expansion of the universe and hence provides a distance measure. Therefore, observations of H I and CO at high redshift are currently discussed as a means of localizing high-redshift galaxies (Carilli & Blain 2002; Carilli & Rawlings 2004), thus unveiling an unprecedented image of cosmic structure (e.g., Abdalla et al. 2009).

However, due to current sensitivity limitations, no H I emission has yet been found beyond redshift $z = 0.25$ (Verheijen et al. 2007; Catinella et al. 2008). In contrast, CO-emission lines have been detected in different systems out to $z \approx 6.4$ (Walter et al. 2004), yet all these lines originate from atypical objects, such as ultraluminous infrared galaxies (ULIRGs) or quasi-stellar objects (QSOs), with the exception of two ordinary galaxies recently detected in CO(2–1) emission at $z \approx 1.5$ (Daddi et al. 2008). Both H I (Prochaska et al. 2005) and H_2 (Noterdaeme et al. 2008) have also been measured via absorption of their respective Lyman lines against distant QSOs. Yet, the nature of the absorbing galaxies remains unknown.

The discrepancy between the primordial astrophysical importance of cold gas in galaxies and its gravely limited detectability at high redshift is a main driver for the design of many future radio and (sub)millimeter telescopes. Prominent examples are the Square Kilometre Array (SKA), the Large Millimeter Telescope (LMT), and the Atacama Large Millimeter/Submillimeter Array (ALMA), which are expected to detect H I and CO at high z. The optimization of these instruments and the planning of their surveys require robust predictions of the detectable signatures. Such predictions are available for the continuum radiation of a large sample of galaxies (e.g., Wilman et al. 2008). By contrast, high-redshift line emission of H I and CO has only been simulated for single galaxies (Boomsma et al. 2002; Combes et al. 1999; Greve & Sommer-Larsen 2008) or simplistically extrapolated for a population of regular galaxies (Blain et al. 2000; Carilli & Blain 2002; Abdalla & Rawlings 2005). All these models ignore the implications of galaxy mergers, cooling flow suppression mechanisms, and other complex phenomena. Moreover, most line simulations exclusively consider either the atomic or the molecular gas phase of the ISM. This approach implicitly assumes that the other phase is negligible or that the masses in both phases evolve proportionally. Both of these assumptions contradict recent studies of the co-evolution of H I and H_2 in regular galaxies (Obreschkow & Rawlings 2009b). Finally, the line simulations cited above neglect cosmic large-scale structure. The time seems ripe for joint predictions of atomic and molecular emission lines in a sample of galaxies large enough to probe cosmic structure.

In this paper, we present a simulation of a sky field with a comoving diameter of $500\,h^{-1}$ Mpc. The actual field of view depends on the (user-defined) maximal redshift z_{max};

* http://s-cubed.physics.ox.ac.uk/, go to "S^3-SAX-Sky"

e.g., for $z_{\max} = 1$ the field of view yields $\sim 12 \times 12$ deg^2, or for $z_{\max} = 10$ the field of view yields $\sim 4 \times 4$ deg^2. This simulation is obtained by constructing a mock observing cone from a previously presented galaxy simulation. The latter relies on the large-scale structure computed by the Millennium Simulation (Springel et al. 2005) and an enhanced semi-analytic galaxy model (Croton et al. 2006; De Lucia & Blaizot 2007; Obreschkow et al. 2009a).

Section 2 explains the simulation methods. In Section 3, we provide a graphical illustration of the simulated sky field and extract dN/dz estimates for peak flux density limited surveys. Section 4 discusses some important limitations of the presented simulation. A non-exhaustive list of possible applications is provided in Section 5 along with a brief conclusion. The appendices show additional illustrations, list the parameters describing the analytic fits to the predicted dN/dz functions, and describe the on-line access to the simulation data.

2. METHODS

In this section, we describe the multiple simulation steps required to progress from a simulation of the *evolution* of cosmic structure to a *static* sky simulation. We have grouped this description into four steps, corresponding to four successive simulation steps. The first step (Section 2.1) contains all the simulation work presented in earlier studies. This work resulted in a catalog of $\sim 3 \times 10^7$ evolving galaxies with detailed cold gas properties. In the second step (Section 2.2), this catalog is transformed into a mock observing cone, which represents a virtual sky field. In the third step (Section 2.3), the intrinsic properties of the galaxies in this virtual sky field are converted into apparent line fluxes. In the fourth step (Sections 2.4 and 2.5), the line emission is refined by the evaluation of line profiles and angular sizes of the line-emitting gas.

2.1. Simulation of the ISM in $\sim 3\times 10^7$ Evolving Galaxies

Here, we recapitulate the galaxy simulation presented in earlier studies. This simulation relies on three consecutive layers: (1) a simulation of the cosmic evolution of dark matter (Springel et al. 2005); (2) a semi-analytic simulation of the evolution of galaxies on the dark matter skeleton (Croton et al. 2006; De Lucia & Blaizot 2007); and (3) a post-processing to split the cold hydrogen masses associated with each galaxy into H I and H_2 (Obreschkow et al. 2009a).

For the dark matter simulation, we adopted the Millennium Simulation (Springel et al. 2005), an *N*-body dark matter simulation within the standard Λ cold dark matter (ΛCDM) cosmology. This simulation uses a cubic simulation box with periodic boundary conditions and a comoving volume of $(500\,h^{-1}\,\mathrm{Mpc})^3$. The Hubble constant was fixed to $H_0 = 100\,h$ km s^{-1} Mpc^{-1} with $h = 0.73$. The other cosmological parameters were chosen as $\Omega_{\mathrm{matter}} = 0.25$, $\Omega_{\mathrm{baryon}} = 0.045$, $\Omega_\Lambda = 0.75$, and $\sigma_8 = 0.9$. The simulation box contains $\sim 10^{10}$ particles with individual masses of $8.6 \times 10^8\ M_\odot$. This mass resolution allows the identification of structures as low in mass as the Small Magellanic Cloud (see Springel et al. 2005).

For the second simulation layer, i.e., the cosmic evolution of the galaxies distributed on the dark matter skeleton, we adopt the semi-analytic model of De Lucia & Blaizot (2007) (see also Croton et al. 2006). In this macroscopic model, all galaxies are represented by a list of global properties, such as position, velocity, and total masses of gas, stars, and black holes. These properties are evolved using empirically or theoretically motivated formulae for mechanisms, such as gas cooling, reionization, star formation, gas heating by supernovae, starbursts, black hole accretion, black hole coalescence, and the formation of stellar bulges via disk instabilities. The resulting virtual galaxy catalog (hereafter the "DeLucia-catalog") contains the positions, velocities, merger histories, and intrinsic properties of $\sim 3 \times 10^7$ galaxies at 64 cosmic time steps. The free parameters in the semi-analytic model were tuned to various observations in the local universe (see Croton et al. 2006). Therefore, despite the simplistic implementation and the possible incompleteness of this model, the DeLucia-catalog nonetheless provides a good fit to the joint luminosity/color/morphology distribution of observed low-redshift galaxies (Cole et al. 2001; Huang et al. 2003; Norberg et al. 2002), the bulge-to-black hole mass relation (Häring & Rix 2004), the Tully–Fisher relation (Giovanelli et al. 1997), and the cold gas metallicity as a function of stellar mass (Tremonti et al. 2004).

In this paper, we are particularly interested in the cold gas masses of the galaxies in the DeLucia-catalog. These cold gas masses are the net result of (1) gas accretion by cooling from a hot halo (dominant mode) and galaxy mergers, (2) gas losses by star formation and feedback from supernovae, and (3) cooling flow suppression by feedback from accreting black holes. The DeLucia-catalog does not distinguish between molecular and atomic cold gas, but simplistically treats all cold gas as a single phase. The atomic and molecular phases are therefore dealt with in the third simulation layer.

The third simulation layer, i.e., the subdivision of the cold hydrogen mass of each galaxy into H I and H_2 distributions (Obreschkow et al. 2009a), relies on an analytic model for the mass distributions of H I and H_2 within regular galaxies. In this model, the column densities of H I and H_2, $\Sigma_{\mathrm{H\,I}}$ and Σ_{H_2}, respectively, are given by

$$\Sigma_{\mathrm{H\,I}}(r) = \frac{\tilde{\Sigma}_{\mathrm{H}}\ \exp(-r/r_{\mathrm{disk}})}{1 + R^{\mathrm{c}}_{\mathrm{mol}} \exp(-1.6\,r/r_{\mathrm{disk}})}\,, \tag{1}$$

$$\Sigma_{H_2}(r) = \frac{\tilde{\Sigma}_{\mathrm{H}}\ R^{\mathrm{c}}_{\mathrm{mol}}\ \exp(-2.6\,r/r_{\mathrm{disk}})}{1 + R^{\mathrm{c}}_{\mathrm{mol}} \exp(-1.6\,r/r_{\mathrm{disk}})}\,, \tag{2}$$

where r denotes the galactocentric radius, r_{disk} is a scale length, $R^{\mathrm{c}}_{\mathrm{mol}}$ is the H_2/H I mass ratio at the galaxy center, and $\tilde{\Sigma}_{\mathrm{H}}$ is a normalization factor. We derived Equations (1) and (2) based on a list of empirically supported assumptions, the most important of which are: (1) the cold gas of regular galaxies resides in a flat disk (see Leroy et al. 2008 for local spiral galaxies, Young 2002 for local elliptical galaxies, Tacconi et al. 2006 for galaxies at higher redshifts); (2) the surface density of the total hydrogen component (H I+H_2) is well described by an axially symmetric exponential profile (Leroy et al. 2008); (3) the local H_2/H I mass ratio scales as a power of the gas pressure of the ISM outside molecular clouds (Blitz & Rosolowsky 2006).

Using Equations (1) and (2), we can characterize the H I- and H_2-content of every simulated galaxy in the DeLucia-catalog. The resulting hydrogen simulation successfully reproduces many local observations of H I and H_2, such as mass functions (MFs), mass–diameter relations, and mass–velocity relations (Obreschkow et al. 2009a). This success is quite surprising, since our model for H I and H_2 only introduced one additional free parameter to match the observed average space density of cold gas in the local universe (Obreschkow et al. 2009a). A key prediction of this simulation is that the H_2/H I ratio of

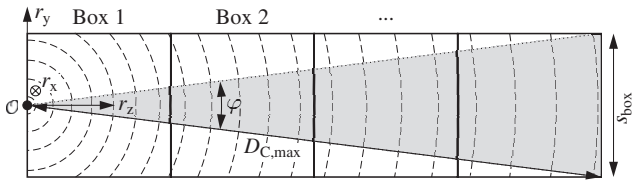

Figure 1. Schematic illustration of the construction of a mock observing cone (shaded region) from a chain of replicated simulation boxes (solid square boxes). The galaxies in the replicated boxes are drawn from the discrete cosmic time step of the simulation, which best corresponds to their cosmological redshift relative to the observer $\mathcal{O}$. Galaxies from the same discrete time step therefore lie within spherical shells around the observer (indicated by the dashed lines).

most regular galaxies increases dramatically with redshift, hence causing a clear signature of cosmic downsizing in the H_2-MF (Obreschkow & Rawlings 2009b).

Despite its consistency with existing observations, we emphasize that the presented model for the cosmic evolution of H I and H_2 is simplistic and uncertain. In particular, at high z, the model assumptions may significantly differ from the reality. For example, high-z galaxies are likely to be more disturbed due to higher merger rates and long dynamic timescales compared to their age. There is also evidence that cold gas disks become more turbulent with redshift (e.g., Förster Schreiber et al. 2006; Genzel et al. 2008). Uncertainties from these and other model limitations are discussed briefly in Section 4 and in depth in Section 6 of Obreschkow et al. (2009a).

2.2. Building a Mock Observing Cone

We shall now describe how the cubic simulation box is transformed into a virtual sky field. This procedure can be regarded as a fourth simulation layer on top of the hierarchical simulation described in Section 2.1.

The method adopted here closely follows the one described by Blaizot et al. (2005), namely the building of a chain of replicated simulation boxes along the line of sight, as shown in Figure 1. At any position in this chain, the galaxies are drawn from the cosmic time in the simulation, which corresponds to the look-back time, at which the galaxy is seen by the observer $\mathcal{O}$. Since our galaxy simulation uses 64 discrete time steps, we describe each galaxy in the cone by its properties at the closest available time step,[3] in terms of redshift. This defines the spherical shells of identical cosmic time, which are separated by dashed lines in Figure 1. The relatively narrow redshift separation of these shells ensures that the assigned galaxy properties cannot differ significantly from the properties at their exact look-back time.

The same galaxy can appear once in every box in Figure 1, but with different intrinsic properties due to the cosmic evolution. However, the position of the repeated galaxy in comoving coordinates will be very similar, which can result in spurious radial features for the observer $\mathcal{O}$ (see Figure 1 in Blaizot et al. 2005). To suppress this effect, we randomize the galaxy positions by applying random symmetry operations to each box in the chain. These operations consist of 90° rotations, inversions, and continuous translations.[4] Applying these symmetry operations also removes the non-physical periodicity of $500\,h^{-1}$ Mpc associated with the side length of the periodic simulation box. But we emphasize that applying the symmetry operations does not provide

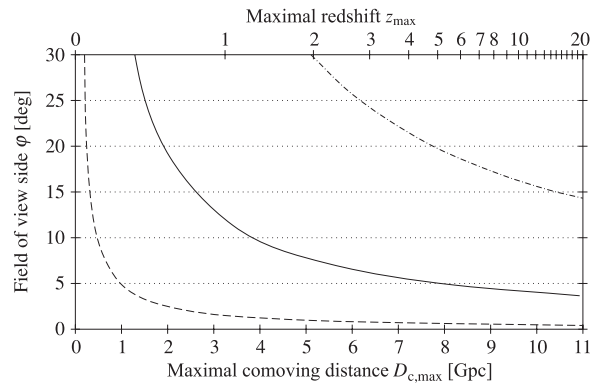

Figure 2. Relation between the maximal comoving distance $D_{C,max}$ or maximal redshift z_{max} and the opening angle φ of the mock observing cone. The different lines correspond to the box sizes of the Millennium Simulation (solid), the Milli-Millennium Simulation (dashed), and the Horizon-4π Simulation (dash-dotted).

information on scales larger than the simulation box. Symmetry operations can, however, introduce unwanted small-scale density variations at the interface of two neighboring boxes. These and other limitations of this method are discussed by Blaizot et al. (2005).

From the randomized chain of replicated simulation boxes, an observing cone can be extracted (shaded region in Figure 1). Each galaxy in this cone is projected onto the celestial sphere centered about the vernal point (R.A. = 0, decl. = 0). The Euclidian projection formulas for arbitrary large angles are

$$\text{R.A.} = \arctan\left(\frac{r_x}{r_z}\right), \tag{3}$$

$$\text{decl.} = \arctan\left(\frac{r_y}{\sqrt{r_x^2 + r_z^2}}\right), \tag{4}$$

where r_x, r_y, and r_z are the comoving coordinates of the galaxy relative to the observer (see Figure 1). The "cosmological redshift" z of each galaxy is computed directly from its comoving distance $D_C = (r_x^2 + r_y^2 + r_z^2)^{1/2}$, while the Doppler-shift-corrected "apparent redshift" is computed as $\tilde{z} = z + V_r/c$, where V_r is the peculiar recession velocity of the galaxy relative to the Hubble flow.

Figure 1 shows that the opening angle φ of the virtual sky field is set by the maximal comoving distance $D_{C,max}$ via

$$\varphi = 2 \arcsin \frac{s_{box}}{2\, D_{C,max}}, \tag{5}$$

where s_{box} is the comoving side length of the simulation box. Given a value of s_{box} and a choice of cosmological parameters, Equation (5) implies a one-to-one relation between φ and the maximal redshift z_{max}.

Figure 2 displays the relation between φ, $D_{C,max}$, and z_{max} for the cosmological parameters of the Millennium Simulation (Section 2.1) and three different side lengths s_{box}. The choice $s_{box} = 500\,h^{-1}$ Mpc (solid line) corresponds to the box of the Millennium Simulation. $s_{box} = 62.5\,h^{-1}$ Mpc (dashed line) corresponds to the "Milli-Millennium" Simulation, a small test version of the Millennium Simulation. $s_{box} = 2\,h^{-1}$ Gpc (dash-dotted line) corresponds to the giant simulation box of the Horizon-4π Simulation, a dark matter stimulation with $\sim$ 10 times less mass resolution than the Millennium Simulation (Prunet et al. 2008; Teyssier et al. 2009; see also Section 4.4).

[3] The galaxy properties cannot readily be interpolated between two successive time steps, since a galaxy at any time step may have several progenitors.

[4] Translations can be applied because of the periodic boundary conditions imposed on the simulation box of the Millennium Simulation.

2.3. Assigning Apparent Line Fluxes

We shall now assign apparent line fluxes to each galaxy in the mock observing cone constructed in Section 2.2. In general, the frequency-integrated line flux S of any emission line can be computed from the frequency-integrated luminosity (= intrinsic power) via

$$S = \frac{L}{4\pi D_{\rm L}^2}, \tag{6}$$

where $D_{\rm L} = (1+z)\, D_{\rm C}$ is the luminosity distance to the source. We note that Equation (6) takes a different form for velocity-integrated fluxes and brightness temperatures. For reference, a summary of all relations between frequency-integrated and velocity-integrated fluxes, luminosities, and brightness temperatures has been compiled in Appendix A of Obreschkow et al. (2009b).

In Sections 2.3.1 and 2.3.2, we shall summarize the models used to estimate the frequency-integrated luminosities L (hereafter simply "luminosities") of different emission lines.

2.3.1. Conversion of H I Mass into H I-line Luminosities

We evaluate the H I luminosities $L_{\rm H\,I}$ from the H I masses $M_{\rm H\,I}$ of the simulated galaxies via the standard conversion (e.g., Meyer et al. 2004)

$$\frac{L_{\rm H\,I}}{L_\odot} = 6.27 \times 10^{-9} \cdot \frac{M_{\rm H\,I}}{M_\odot}. \tag{7}$$

The H I line or "21 cm line" at a rest-frame frequency of 1.420 GHz originates from the photon-mediated transition between the two spin states of the proton–electron system in the electronic ground state. The upper spin state has a low spontaneous decay rate of $f = 2.9 \times 10^{-15}$ Hz. This frequency is about five orders of magnitude smaller than that of H I–H I collisions (Binney & Merrifield 1998). Hence, the two spin states are in thermal equilibrium with the kinetic state of the gas, which implies a spin-temperature far above the spin excitation temperature $T_{\rm ex} \approx 0.07$ K. Therefore, the spin systems are in the high-temperature limit, where 3/4 of all systems are in the upper (three-fold degenerate) state. The radiative power emitted per atom can therefore be calculated as $L_{\rm H\,I} = 0.75\, f\, h_{\rm p}\, 1.4$ GHz ($h_{\rm p}$ is the Planck constant), which readily reduces to Equation (7).

We have neglected H I self-absorption, since this seems to affect only massive spiral galaxies when observed almost edge-on (Ferrière 2001; Wall 2006). This assumption should also be valid for high-redshift galaxies, since their H I masses were not much larger than today, as can be inferred from Lyα-absorption measurements against distant quasars (Lah et al. 2007) and as is predicted by our simulation (Obreschkow & Rawlings 2009b).

H I in collapsed structures, i.e., in galaxies, is generally warm enough ($\gtrsim$ 50 K) that the Cosmic Microwave Background (CMB) can be safely neglected as an observing background for all galaxies at $z < 10$. Only in the intergalactic medium (IGM) during the cosmic Epoch of Re-ionization (EoR) can H I appear in 21 cm absorption against the CMB (e.g., Iliev et al. 2002).

2.3.2. Conversion of H_2 Mass into CO-line Luminosities

We derive the CO-line luminosities $L_{\rm CO}$ from the H_2 masses of the simulated galaxies. We only consider the radiation emitted by the most abundant CO isotopomer, $^{12}C^{16}O$, when relaxing from one of the rotational states $J = 1, \ldots, 10$ to the state $J-1$. The radiation frequency of such a decay is $J \cdot \nu_{\rm CO}$, where $\nu_{\rm CO} = 115.27$ GHz is the rest-frame frequency of the transition $J = 1 \rightarrow 0$.

The conversion between H_2 masses and CO luminosities is a highly nuanced affair with a long history in millimeter astronomy. We therefore presented an in-depth analysis of this conversion in Obreschkow et al. (2009b) and introduced a model to estimate the different luminosities $L_{\rm CO,J}$ of the galaxies in our simulation. This model respects the following physical mechanisms: (1) molecular gas is heated by the CMB, starbursts (SBs), and active galactic nuclei (AGNs); (2) molecular clouds in dense or inclined galaxies can overlap; (3) very dense gas is smooth instead of clumpy; (4) the metallicity varies amongst galaxies and changes with redshift; (5) CO luminosities are always detected against the CMB. We shall apply this model in the present paper. Limitations and uncertainties are discussed in Section 4.3.

2.4. Emission Line Profiles

Having assigned an integrated line flux to each galaxy in the simulation, we can now refine their attributes by characterizing each line with a profile. To this end, we depart from the *edge-on* line profiles evaluated in Obreschkow et al. (2009a) for each galaxy in the simulation. We represented those profiles by normalized flux densities $\Psi(V)$, where V is the velocity measured in the rest frame of the center of the observed galaxy. The normalization condition, $\int_{\rm V} \Psi(V) dV = 1$, implies that $\Psi(V)$ only needs to be multiplied by the velocity-integrated flux (in units of Jy km s^{-1}) in order to obtain actual flux densities (in units of Jy). For each galaxy, we calculated two profiles $\Psi(V)$, one for the H I component and one for the H_2 component (associated with CO).[5] This calculation relied on a detailed mass model based on the halo, disk, and bulge of the galaxies, combined with our model for the H I- and H_2-surface densities given in Equations (1) and (2). For practical reasons, the resulting line profiles were reduced to five parameters (see Figure 8): the normalized flux density at the line center Ψ_0; the normalized peak flux density $\Psi_{\rm max}$, usually corresponding to the two peaks of a double-horn profile; the line width $w_{\rm peak}$ between the two peaks of the double-horn profile; the line width w_{50} at the 50 percentile level of the peak flux density; and the line width w_{20} at the 20 percentile level. The original normalized line profile can be approximately recovered from these parameters using the formulas in Appendix A.

The remaining task consists of correcting the line profiles for the inclination i of each galaxy.[6] i is defined as the angle between the line of sight and the galaxy's rotation axis; hence $i = 0°$ corresponds to face-on galaxies and $i = 90°$ corresponds to edge-on galaxies. In the absence of a random gas velocity dispersion, apparent line widths $w^{\rm obs}$ could be computed from the edge-on line widths w, via $w^{\rm obs} = w \cdot \sin i$, while apparent normalized flux densities would scale as $\Psi^{\rm obs} = \Psi / \sin i$.

Here, we assume that the cold gas has a random, isotropic velocity dispersion characterized by a Gaussian velocity distribution in each space dimension. The observed line profile of a face-on galaxy ($i = 0°$) then takes the shape of a Gaussian function. Under no inclination can the line profile become more narrow than this Gaussian function, nor can the normalized line

[5] In Obreschkow et al. (2009a), we called these two profiles $\Psi_{\rm H\,I}$ and $\Psi_{\rm CO}$, respectively.

[6] The simulated DeLucia-catalog does not provide galaxy orientations. We therefore assign inclinations randomly between 0° (face-on) and 90° (edge-on) according to a sine-distribution.

flux densities become higher than the peak of this Gaussian function. Let σ be the standard deviation of the Gaussian velocity dispersion. Then the minimum line widths are given by $w_{20}^{\rm obs} = 2\sqrt{-2\ \ln(0.2)} \approx 3.6\,\sigma$, $w_{50}^{\rm obs} = 2\sqrt{-2\ \ln(0.5)} \approx 2.4\,\sigma$, and $w_{\rm peak}^{\rm obs} = 0$, and the maximum normalized flux densities are $\Psi_0 = (\sigma\sqrt{2\pi})^{-1}$ and $\Psi_{\rm max} = (\sigma\sqrt{2\pi})^{-1}$.

In addition, the maximal normalized flux density $\Psi_{\rm max}$ cannot differ from the central normalized flux density Ψ_0 by an arbitrarily large amount due to the line profile smoothing. Explicitly, the slope in the emission line between the points Ψ_0 and $\Psi_{\rm max}$ cannot exceed the maximal slope of the Gaussian velocity function, which is equal to $0.24\,\sigma^{-2}$. This requirement translates into an upper bound for $\Psi_{\rm max}$ equal to $\Psi_0^{\rm obs} + 0.12\,\sigma^{-2}\,w_{\rm peak}^{\rm obs}$. A set of equations respecting all of these conditions is given by

$$w_{20}^{\rm obs} = (w_{20} - 3.6\,\sigma)\cdot \sin i + 3.6\,\sigma, \tag{8}$$

$$w_{50}^{\rm obs} = (w_{50} - 2.4\,\sigma)\cdot \sin i + 2.4\,\sigma, \tag{9}$$

$$w_{\rm peak}^{\rm obs} = w_{\rm peak}\cdot \sin i, \tag{10}$$

$$\Psi_0^{\rm obs} = \min\left(\frac{\Psi_0}{\sin i}, \frac{1}{\sigma\sqrt{2\pi}}\right), \tag{11}$$

$$\Psi_{\rm max}^{\rm obs} = \min\left(\frac{\Psi_{\rm max}}{\sin i}, \frac{1}{\sigma\sqrt{2\pi}}, \Psi_0^{\rm obs} + \frac{0.12 w_{\rm peak}^{\rm obs}}{\sigma^2}\right). \tag{12}$$

For all the line profiles, we here adopt $\sigma = 8$ km s^{-1} to remain consistent with Obreschkow et al. (2009a). We note, however, that high-redshift galaxies may have higher velocity dispersions (Förster Schreiber et al. 2006) perhaps due to an intense ongoing accretion of gas. Another limitation of the presented line model is that all CO lines have by definition the same line shape. This assumption nevertheless approximately agrees with simultaneous observations of different emission lines (e.g., Weiss et al. 2007; Greve et al. 2009).

2.5. Angular Sizes

We shall finalize our simulation of line-emitting galaxies by ascribing an angular distribution (flux per unit solid angle) in the sky to each emission line. To this end, we assume that, for a fixed galaxy, the angular distributions of the H I flux and the different CO fluxes are proportional to the angular distributions of H I and H_2, respectively. We emphasize, however, that the conversion factor between H_2 masses and CO fluxes depend on the J level of the CO transition and on the galaxy, such as outlined in Section 2.3.2.

Given this assumption, we can infer the line flux densities per unit solid angle from the surface densities $\Sigma_{\rm H\,I}(r)$ and $\Sigma_{\rm H_2}(r)$ given in Equations (1) and (2). We only need to normalize these densities to the respective line fluxes and to replace the scale radius $r_{\rm disk}$ by the apparent scale radius $r_{\rm disk}/D_{\rm A}$, where $D_{\rm A} = (1+z)^{-1}\,D_{\rm C}$ is the angular diameter distance.

The shapes of the line-emitting regions need to be corrected for the inclinations i. If $q_{\rm HI,0}$ and $q_{\rm H_2,0}$ respectively denote the intrinsic axis ratios of the atomic and molecular gas in galaxies, then the apparent axis ratios are given by (Equation (1) in Kannappan et al. 2002)

$$q_{\rm H\,I}^2 = \cos^2 i + q_{\rm HI,0}^2\,\sin^2 i, \tag{13}$$

$$q_{\rm H_2}^2 = \cos^2 i + q_{\rm H_2,0}^2\,\sin^2 i. \tag{14}$$

These relations satisfy $q_{\rm H\,I} = q_{\rm H_2} = 1$, if $i = 0^\circ$ (face-on), and $q_{\rm H\,I} = q_{\rm HI,0}$ and $q_{\rm H_2} = q_{\rm H_2,0}$, if $i = 90^\circ$ (edge-on).

We assume that all galaxies have the same values for respectively $q_{\rm HI,0}$ and $q_{\rm H_2,0}$. In local spiral galaxies, we typically find $q_{\rm HI,0} = 0.1$, as can be seen from high-resolution maps of the edge-on spiral galaxies NGC 891 and NGC 4565 (Rupen 1991). To our knowledge, no reliable estimate of $q_{\rm H_2,0}$ for disk galaxies is available. However, simultaneous CO(1–0) and optical observations revealed that the density of stars in nearby galaxies correlates with the density of molecular gas, when averaged over sufficiently large (> kcp) scales (Richmond & Knapp 1986; Leroy et al. 2008), probably as a natural consequence of the formation of stars from molecular gas. Therefore, we shall assume that the intrinsic aspect ratio of molecular gas $q_{\rm H_2,0}$ is identical to that of stellar disks. The latter is ~ 0.1, as can be seen in the sample of 34 nearby edge-on spiral galaxies studied by Kregel et al. (2002). We therefore adopt $q_{\rm H_2,0} = 0.1$. We stress that $q_{\rm HI,0} = q_{\rm H_2,0}$ does not contradict the fact that characteristic scale radii and scale heights of H I distributions are generally larger than those of H_2 distributions (Leroy et al. 2008).

The assumption of constant values for $q_{\rm HI,0}$ and $q_{\rm H_2,0}$ for all galaxies at all redshifts may not be verified at high redshifts due to timescale arguments. In fact, a significant fraction of the galaxies at $z > 5$ may have an age comparable to their dynamical timescale. Their cold gas distribution might therefore be thicker and less circularly symmetric than the flat gas disks seen today. However, no reliable estimates of $q_{\rm HI,0}$ and $q_{\rm H_2,0}$ beyond the local universe are available today.

3. RESULTS

The simulated mock observing cone can be accessed on-line as described in Appendix B. This section starts with a graphical illustration of the simulated mock observing cone. As a second step, we analyze the predicted number of galaxies detected in an idealized line survey with a constant peak flux density limit. Specific predictions for particular surveys with radio and (sub)millimeter telescopes, such as the SKA, the LMT, and ALMA, will follow in forthcoming studies.

3.1. Graphical Overview

By successively applying the simulation steps described in Section 2, we have constructed an observing cone of line-emitting galaxies. Figure 3 shows a longitudinal slice of this cone with a thickness of 10 Mpc. This slice corresponds to a diagonal cut, as illustrated in Figure 3 and has an opening angle of 5°.8. Each pixel inside this slice corresponds to a galaxy. The structure of the cosmic web appears clearly, as well as the increasing filamentarity of this structure with decreasing redshift. The color scales represent the H_2/H I mass ratios of the galaxies. We can clearly recognize the pressure-driven cosmic decline of this ratio (see Obreschkow & Rawlings 2009b).

The mock observing cone translates into a virtual sky field when projected onto a sphere using Equations (3) and (4). Figure 4 displays the H I- and CO-flux densities of galaxies between $z = 1$ and $z = 1.1$ in a small extract of this virtual sky. The surface densities of the galaxies have been modeled using Equations (1) and (2) in the manner described in Section 2.5. The more massive galaxies in the field reveal ring-like H I distributions with CO-rich central regions. By contrast, some of

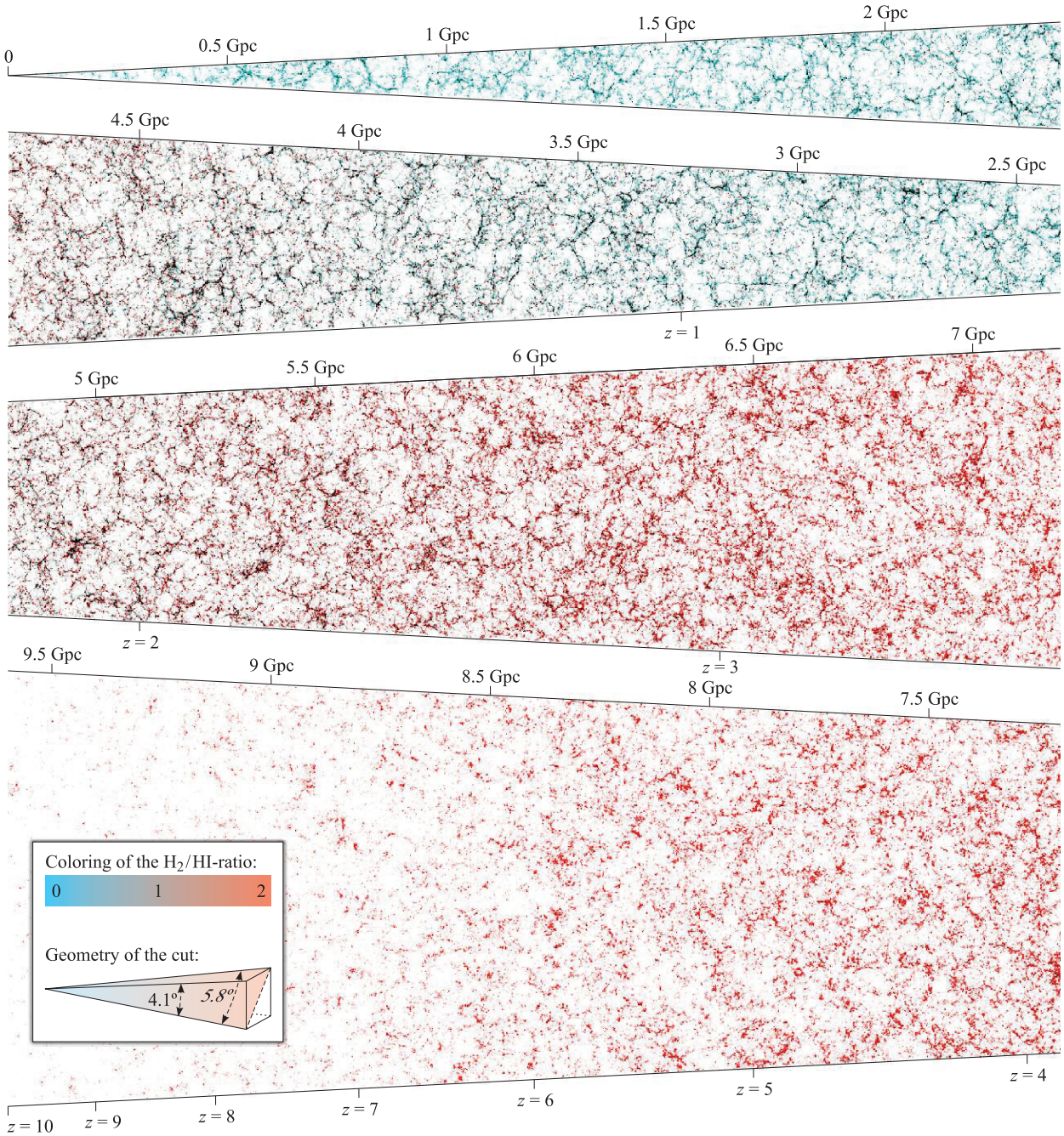

Figure 3. Longitudinal cut through the simulated mock observing cone. The cut slice has a thickness of 10 Mpc and is represented in comoving coordinates. For illustration purposes, the slice has been wrapped in four parts, which variably read from the left to the right and vice versa. The dots represent gas-rich galaxies and the coloring shows their H_2/H I ratio, from 0 (blue) to 2 (red).

the smaller galaxies with low surface brightness (LSB), have most of their H I in the center, with nearly no detectable CO. In general, CO (and hence H_2) is more compact than H I. All these simulated features compare well to observed radial distributions (averaged on suitably large scales) of H I and CO in nearby galaxies (Leroy et al. 2008) as demonstrated in Obreschkow et al. (2009a) and Obreschkow & Rawlings (2009a). Nevertheless, we emphasize that the idealized nature (e.g., axial symmetry) of the simulated galaxies misses out a list of structural features found in many real galaxies, such as spiral arms, warps, and lopsidedness.

The coloring of the CO-surface densities in Figure 4 (right) represents the CO(5–4)/CO(1–0) line ratio in terms of brightness temperatures. For normal galaxies, without a particular source of heating, this ratio is much smaller than unity (yellow coloring); however, for some galaxies with strong heating by an ongoing SB or AGN, the higher order lines can get excited (red coloring). These mechanisms and our model to assess them are discussed in Obreschkow et al. (2009b).

Figure 9 in Appendix C shows a 3 times larger sky field than Figure 4 at the three redshifts $z \approx 1$, $z \approx 3$, and $z \approx 6$. The progression from $z \approx 1$ to $z \approx 6$ in Figure 9 reveals two notable features. Firstly, galaxy sizes decrease with redshift. In fact, the angular diameter distances at $z \approx 1$ and $z \approx 3$ are virtually identical according to the cosmology adopted in this paper (Section 2.1). Therefore, the galaxy sizes of these two virtual sky maps can be compared directly. The angular

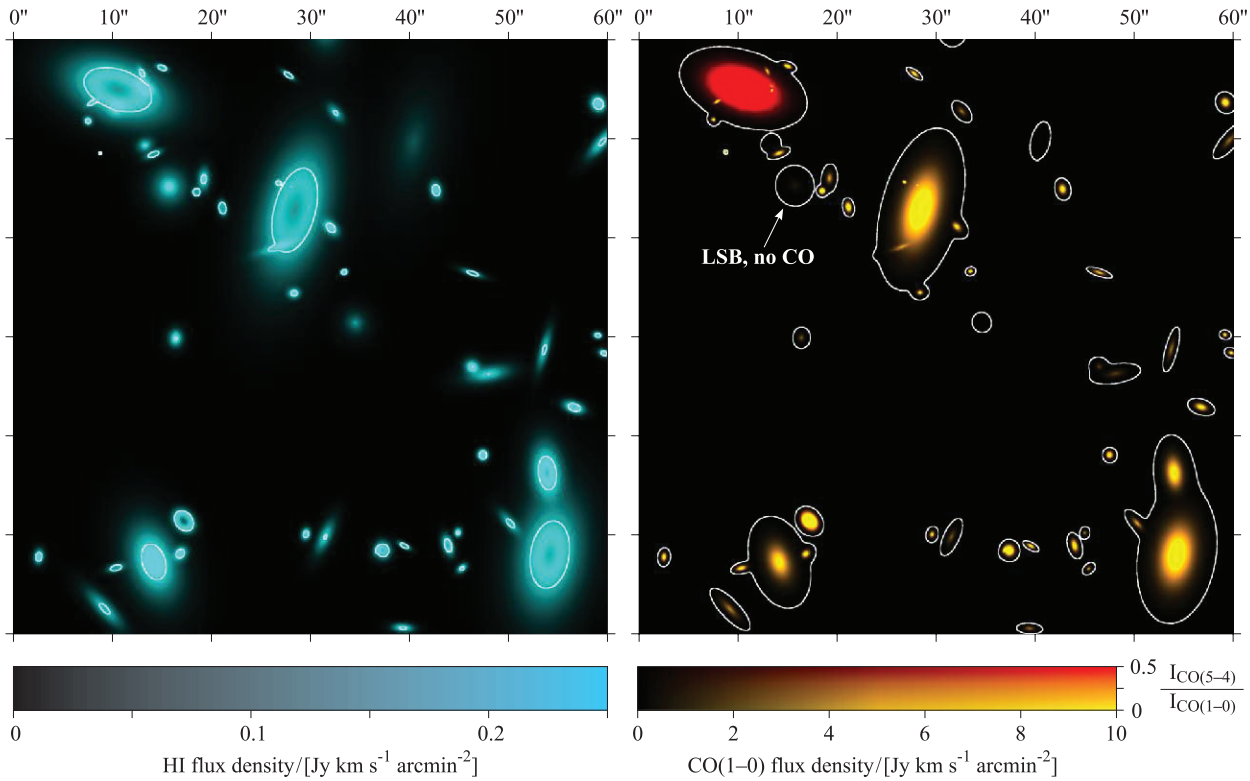

Figure 4. Illustration of the galaxies in the redshift range $z = 1.0$–1.1 in a small field of 1 arcmin^2. The full field of view of the observing cone is 60,000 times larger than this example. The gradual coloring represents integrated line fluxes per unit solid angle for H I (left) and CO(1–0) (right). The different color tones for CO represent the brightness temperature intensity ratio $I_{\mathrm{CO(5-4)}}/I_{\mathrm{CO(1-0)}}$. The white contours around H I sources represent iso-density curves of CO at the 50 percentile level of the full CO density scale and vise versa.

diameter distance at $z \approx 6$ is about 25% smaller, hence the same physical scales appear slightly oversized. The size evolution of the galaxies reflects the cosmic evolution of the volume/mass ratio of the dark matter halos (Gunn & Gott 1972). We discussed the impact of this evolution on the surface densities of H I and H_2 in Obreschkow & Rawlings (2009a).

Secondly, the CO(5–4)/CO(1–0) line ratios of CO-detectable galaxies increases with redshift. In fact, at $z \approx 6$ no galaxy with a line ratio significantly below unity (i.e., with yellow coloring) can be seen. This feature relies partially on the compactness of the galaxies, which, according to our model for CO lines (Obreschkow et al. 2009b), allows an efficient heating by star formation. An additional reason for the absence of low CO(5–4)/CO(1–0) line ratios at $z \gtrsim 6$ is that molecular gas in galaxies with no significant star formation and no AGN will be hardly detectable in CO due to its near thermal equilibrium with the CMB.

3.2. dN/dz for a Peak Flux Density Limited Survey

In the simulated observing cone, we can readily count the number of galaxies per redshift interval with line fluxes above a certain threshold. This dN/dz analysis is a key step toward the prediction of the number of sources detectable with any particular telescope and survey strategy. In this section, we focus on the number of sources detected in a peak-flux-density-limited survey, and we restrict the presented results to the H I-, CO(1–0)-, CO(5–4)-, and CO(10–9)-emission lines. Results for other CO-emission lines and/or for integrated flux limited surveys are presented in Appendix D.

Figure 5 shows the dN/dz functions for six different peak flux density limits, logarithmically spaced between 1mJy and 10nJy. Peak flux densities for each source and emission line are calculated in the way described in Section 2.4. This method accounts for the different gas distributions, rotation curves, and inclinations of the galaxies. Every source with a peak flux density above the peak flux density limit is considered as detected, while all other sources are considered as non-detected. Different aspects of Figure 5 will be discussed in detail over the following paragraphs.

3.2.1. Cosmic Variance

The simulated dN/dz functions shown in Figure 5 (solid and dotted lines) correspond to a bin size of $\Delta z = 0.1$ and a sky field of 4×4 deg^2, extracted from *one particular* realization of the mock observing cone, that is one random choice of symmetry operations for the replicated simulation boxes (see Section 2.2). The wiggles visible in the simulated dN/dz functions are physical. Similar wiggles can be expected for a real sky survey of a sky field of 4×4 deg^2 with a redshift bin size of $\Delta z = 0.1$. The fact that the amplitude of those wiggles does not decrease as $1/\sqrt{dN/dz}$ clearly uncovers the presence of the cosmic large-scale structure, also visible in Figure 3.

To quantify the effects of cosmic variance, we now consider the dN/dz functions extracted from five different random realizations of the mock observing cone. Figure 6 shows the corresponding dN/dz functions for a peak flux limited H I survey with a peak flux limit of 1μJy. Each function uses a bin size of $\Delta z = 0.1$ and a small sky field of 1×1 deg^2 in order to make the effects of cosmic structure obvious. As a rough estimate the log-scatter between the different dN/dz functions is about 0.1 dex. From this small scatter, we conclude that cosmic variance is, in most cases, negligible compared to the uncertainties of the semi-analytic galaxy model.

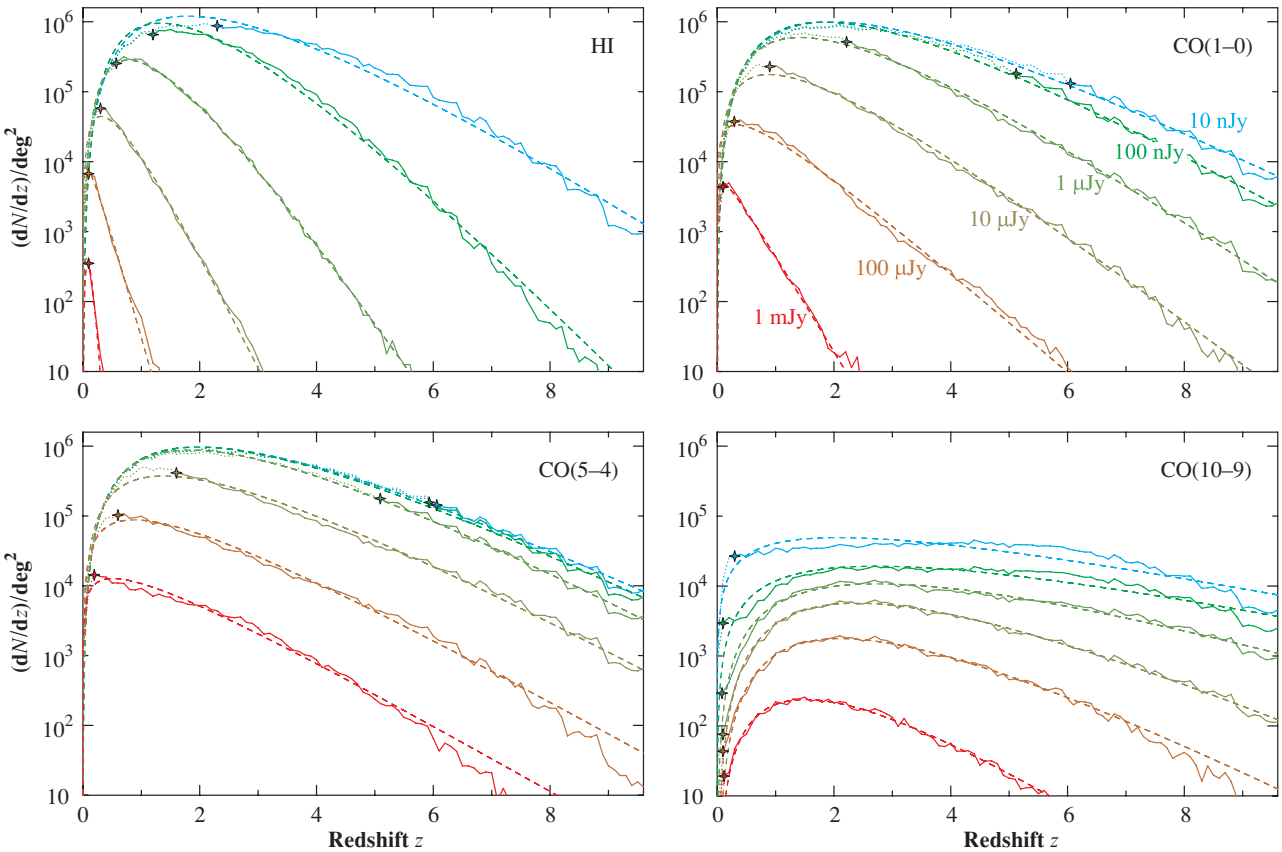

Figure 5. dN/dz plots for the emission lines of H I, CO(1–0), CO(5–4), and CO(10–9) at different peak flux density limits. Solid lines represent the simulated data in the regime where the simulated galaxy sample is complete. Dotted lines represent the cases where the flux density limit is low enough to detect sources in the incomplete parts of the galaxy mass function (see Section 3.2). These dotted lines should be considered as lower limits. To increase the readability, the transitions from the complete regime (solid lines) to the incomplete regime (dashed lines) have been marked with stars. All simulated functions (solid and dotted lines) use a redshift bin size of $\Delta z = 0.1$ and a sky field of 4×4 deg^2, corresponding to a maximal redshift $z_{\max} = 10$. Dashed lines represent analytic fits of Equation (15). The respective fitting parameters are listed in Table 1. Colors correspond to the peak flux density limits shown in the panel for CO(1–0).

(A color version of this figure is available in the online journal.)

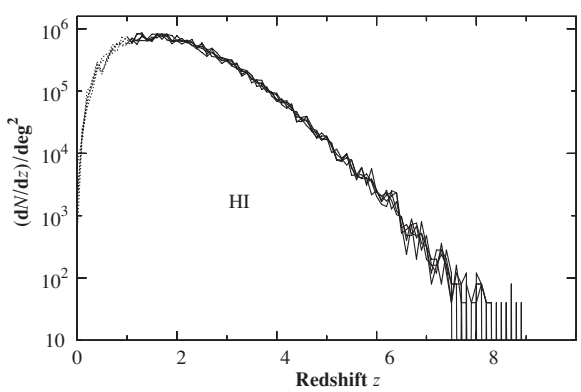

Figure 6. Effects of cosmic variance on a peak-flux-limited H I survey with a flux limit of 1 μJy. The five lines show the dN/dz functions extracted from five distinct random realizations of the mock observing cone (see Section 2.2). Each function uses a bin size of $\Delta z = 0.1$ and a small sky field of 1×1 deg^2 in order to illustrate the effects of cosmic variance.

However, the comoving volume per unit solid angle and unit redshift varies as a function of redshift. Therefore, the scatter due to cosmic variance varies with redshift. It is largest at the lowest redshifts ($z < 0.5$), where the comoving surface per unit solid angle is small, and at the highest redshifts ($z > 5$), where the radial comoving distance per unit of redshift is small. In these redshift regimes, effects of cosmic variance should therefore be estimated, when comparing simulated data to observations.

3.2.2. Completeness

The semi-analytic simulation is complete for galaxies with total hydrogen masses (H I+H$_2$) above $\sim 10^8\ M_\odot$. Galaxies with smaller hydrogen masses typically sit at the centers of halos with less than 20 particles in the Millennium Simulation, which cannot be reliably identified. Therefore, the number of these low-mass galaxies is heavily underestimated by the simulation. In principle, the sensitivity of a line survey can be high enough that galaxies in this incomplete region of the simulated MF are detected.

In fact, for each emission line and each sensitivity limit, there is a critical redshift z_c, below which sources of the incomplete part of the simulated galaxy MF will be detected at a sufficiently high rate that the number of real detections will significantly exceed the number of simulated detections. Therefore, the simulated dN/dz functions at $z \leqslant z_c$ must be considered as lower limits.

We shall here define z_c as the redshift, below which the fraction of sources with hydrogen masses below $10^8\ M_\odot$ becomes larger than 1%. This may seem to be a very low threshold, but we stress that the incomplete part of the simulated hydrogen MF misses a significant fraction of the "real" sources and hence the value of dN/dz may be underestimated by much more than 1% if $z \leqslant z_c$. In Figure 5, the values of z_c have been marked with stars, and the simulated dN/dz functions at $z \leqslant z_c$ have been plotted as dotted lines instead of solid ones.

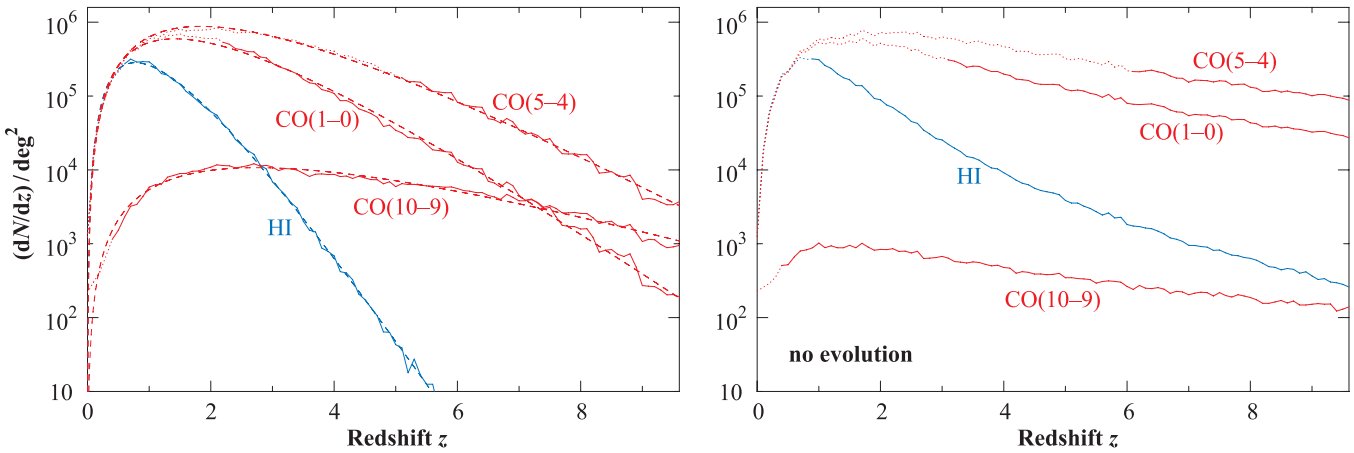

Figure 7. Comparison of the dN/dz plots for different emission lines observed with an identical peak flux density limit of 1 μJy. The left panel shows our simulation presented in this paper. For comparison, the right panel represents the case of a simulation with no galaxy evolution, as obtained by using only the local galaxy simulation box for the construction of the mock observing cone. The line types are as explained in Figure 5, and colors have been used to distinguish H I (blue) from CO (red). All simulated functions (solid and dotted) use a redshift bin size of $\Delta z = 0.1$ and a sky field of 4×4 deg^2, corresponding to a maximal redshift $z_{\max} = 10$. (A color version of this figure is available in the online journal.)

3.2.3. Parameterization of the dN/dz plots

The simulated dN/dz functions can easily be recovered from the on-line database of the sky simulation (see Appendix B). Alternatively, we also approximated the dN/dz functions by analytic fits of the form

$$\frac{dN/dz}{\mathrm{deg}^2} = 10^{c_1} \cdot z^{c_2} \cdot \exp(-c_3 \cdot z), \qquad (15)$$

where c_1, c_2, and c_3 are free parameters. The best parameters in terms of an rms minimization are shown in Table 1 for various emission lines detected with different limits for the peak flux densities and integrated fluxes. Analytic dN/dz functions for intermediate flux limits can be approximately inferred by linearly interpolating the parameters c_1, c_2, and c_3.

3.2.4. Basic Conclusions

An important conclusion from Figure 5 is that H I surveys at high redshift ($z \gtrsim 2$) will be difficult compared to CO surveys. For example, in order to detect the same number of sources at $z \approx 4$, an H I survey will need to be approximately 10 times more sensitive than a CO(1–0) survey and over 100 times more sensitive than a CO(5–4) survey. However, we emphasize that with single dish receivers this effect is partially offset by the fact that the instantaneous field of view increases as λ^2, where λ is the observed wavelength. This scaling implies that single dish H I surveys are likely to yield much more integration time per unit solid angle, which effectively increases the sensitivity. Furthermore, new technologies, such as aperture arrays (Carilli & Rawlings 2004), are currently being developed to provide an enormous instantaneous field of view and hence a very high effective sensitivity for the detection of H I.

Figure 7 (left) shows a comparison of the simulated dN/dz functions for different emission lines observed with an identical peak flux density limit of 1 μJy. The flat slope of the dN/dz function for CO(10–9) reflects that this line is boosted by SBs, which were more abundant and effective (more compact galaxies) at high z (see Obreschkow et al. 2009b). CO(1–0) reveals the steepest slope of all the CO lines in the dN/dz-plot. On one hand, this feature indicates that local galaxies are dominated by low-order excitations of the CO molecule, consistent with empirical data (Braine et al. 1993). On the other hand, CO(1–0) becomes nearly invisible in normal (i.e., no AGN, no SB) galaxies at high redshift ($z > 7$) due to a near thermal equilibrium between the molecular gas and the CMB (Obreschkow et al. 2009b; see also Combes et al. 1999; Papadopoulos et al. 2000). The even steeper slope of the dN/dz function for H I originates from the cosmic decline of the H_2/H I ratio in galaxies described in Obreschkow & Rawlings (2009b).

Figure 7 (right) shows the same dN/dz functions as Figure 7 (left), but for the case of no galaxy evolution. These functions were obtained by constructing a mock observing cone using only the simulation box at $z = 0$. The comparison of Figure 7 (left) to Figure 7 (right) reveals that H I at high redshifts will be much harder to detect than predicted by a no-evolution model. Qualitatively, the same conclusion applies to low-order CO-emission lines, but the effect is less significant. In contrast, our simulation predicts that the high-order CO-emission lines will be easier to detect than suggested by a no-evolution model, since these lines will be strongly boosted by SBs at high redshift.

4. DISCUSSION

4.1. Limitations of the Galaxy Simulation

Our simulation is inevitably bound to the ΛCDM cosmology with the cosmological parameters given in Section 2. The empirical uncertainty of these parameters may be a source of systematic errors in our predictions. To analyze the errors associated with the uncertainty of the Hubble constant, we can study the change of our predictions in the linear expansion[7] of h. This analysis shows that varying h between 0.6 and 0.8 does not significantly affect the dN/dz functions, i.e., not more than a factor 2. Additionally, Wang et al. (2008) showed that the lower value for the fluctuation amplitude σ_8 found by WMAP-3 compared to the value used in the Millennium Simulation is almost entirely compensated by an increase in halo bias. Caution should nevertheless be applied when relying on predictions from a single cosmological model.

An additional limitation of the Millennium Simulation is the mass resolution of 8.6×10^8 $M_\odot$ per particle. This mass

[7] In the simulation, both masses and lengths scale as h^{-1} (Springel et al. 2005).

Table 1
Parameters for the Analytic Fit Formula of Equation (15) for dN/dz Peak-Flux-Density-Limited and Integrated-Flux-Limited Surveys

Parameters		Limiting Peak Flux Density (Jy)						Limiting Integrated Flux (Jy km s^{-1})					
		10^{-8}	10^{-7}	10^{-6}	10^{-5}	10^{-4}	10^{-3}	10^{-6}	10^{-5}	10^{-4}	10^{-3}	10^{-2}	10^{-1}
H I	c_1	6.55	6.87	6.73	5.75	4.56	6.62	6.61	6.94	6.53	5.79	5.21	6.33
	c_2	2.54	2.85	2.32	1.14	0.43	2.64	2.66	2.91	2.09	1.33	1.23	2.60
	c_3	1.42	2.17	3.09	3.95	6.86	35.49	1.51	2.34	2.86	3.92	8.38	30.52
	z_c	2.3	1.1	0.5	0.2	0.1	0.1	2.1	0.9	0.4	0.1	0.1	0.1
CO(1–0)	c_1	6.32	6.40	6.37	5.92	5.06	4.15	6.31	6.37	6.30	5.91	5.27	5.17
	c_2	2.16	2.29	2.05	1.33	0.54	0.31	2.14	2.23	1.96	1.43	0.95	1.37
	c_3	1.11	1.27	1.46	1.55	1.72	3.46	1.11	1.23	1.38	1.47	1.69	5.19
	z_c	6.0	5.1	2.2	0.9	0.3	0.1	6.0	5.1	2.2	0.9	0.4	0.1
CO(2–1)	c_1	6.29	6.34	6.42	6.25	5.64	4.64	6.29	6.33	6.38	6.21	5.67	4.87
	c_2	2.10	2.20	2.27	1.81	1.07	0.35	2.09	2.18	2.18	1.84	1.23	0.70
	c_3	1.07	1.15	1.34	1.51	1.58	1.94	1.06	1.14	1.28	1.46	1.49	1.82
	z_c	5.8	6.0	3.8	1.5	0.6	0.2	5.8	6.0	3.8	1.5	0.6	0.2
CO(3–2)	c_1	6.28	6.32	6.40	6.32	5.79	4.86	6.28	6.31	6.37	6.25	5.81	5.09
	c_2	2.08	2.16	2.27	1.95	1.22	0.47	2.08	2.14	2.21	1.89	1.36	0.87
	c_3	1.06	1.12	1.27	1.44	1.48	1.58	1.06	1.11	1.23	1.36	1.43	1.56
	z_c	5.8	6.0	4.9	2.0	0.7	0.3	5.8	6.0	4.7	2.0	0.8	0.3
CO(4–3)	c_1	6.28	6.31	6.37	6.26	5.74	4.84	6.28	6.30	6.34	6.19	5.77	5.03
	c_2	2.08	2.13	2.22	1.87	1.18	0.52	2.08	2.12	2.17	1.79	1.34	0.86
	c_3	1.06	1.10	1.21	1.32	1.36	1.38	1.06	1.09	1.18	1.25	1.33	1.36
	z_c	5.8	6.0	5.2	2.1	0.7	0.3	5.8	6.0	5.2	2.0	0.8	0.3
CO(5–4)	c_1	6.28	6.30	6.32	6.05	5.45	4.53	6.28	6.29	6.30	6.00	5.53	4.74
	c_2	2.07	2.11	2.13	1.56	0.96	0.54	2.07	2.11	2.09	1.52	1.20	0.83
	c_3	1.05	1.09	1.17	1.15	1.14	1.14	1.05	1.08	1.15	1.09	1.17	1.15
	z_c	5.8	6.0	5.1	1.7	0.6	0.2	5.8	6.0	4.7	1.6	0.6	0.2
CO(6–5)	c_1	6.28	6.29	6.17	5.62	4.95	4.17	6.28	6.28	6.13	5.62	5.08	4.35
	c_2	2.07	2.09	1.81	1.04	0.78	0.93	2.07	2.07	1.76	1.11	1.02	1.13
	c_3	1.05	1.09	1.07	0.89	0.92	1.08	1.05	1.08	1.03	0.87	0.97	1.06
	z_c	5.8	6.0	6.2	0.9	0.3	0.1	5.8	6.0	6.0	0.9	0.4	0.1
CO(7–6)	c_1	6.27	6.22	5.72	5.01	4.45	3.91	6.27	6.20	5.70	5.08	4.55	4.06
	c_2	2.06	1.96	1.14	0.69	1.13	1.58	2.05	1.93	1.18	0.80	1.18	1.72
	c_3	1.05	1.06	0.80	0.65	0.88	1.24	1.05	1.04	0.79	0.66	0.86	1.14
	z_c	6.0	5.2	1.3	0.4	0.2	0.1	6.0	5.2	1.2	0.4	0.1	0.1
CO(8–7)	c_1	6.22	5.76	5.00	4.42	4.13	3.68	6.20	5.74	5.08	4.48	4.19	3.78
	c_2	1.97	1.25	0.66	1.04	1.85	2.22	1.95	1.27	0.80	0.99	1.83	2.06
	c_3	1.04	0.78	0.51	0.62	1.03	1.45	1.02	0.78	0.55	0.58	0.97	1.19
	z_c	6.0	6.6	0.5	0.2	0.1	0.1	6.0	1.3	0.5	0.2	0.1	0.1
CO(9–8)	c_1	5.70	4.95	4.35	4.10	3.84	3.33	5.69	5.03	4.43	4.12	3.93	3.43
	c_2	1.24	0.74	1.05	1.81	2.31	2.17	1.27	0.87	1.04	1.70	2.20	2.27
	c_3	0.73	0.46	0.48	0.81	1.14	1.43	0.73	0.51	0.48	0.73	1.04	1.21
	z_c	6.2	0.4	0.1	0.1	0.1	0.1	1.2	0.4	0.1	0.1	0.1	0.1
CO(10–9)	c_1	4.81	4.29	4.03	3.88	3.52	2.95	4.89	4.35	4.07	3.91	3.65	3.00
	c_2	0.86	1.29	1.80	2.29	2.27	2.23	0.95	1.26	1.76	2.21	2.35	2.03
	c_3	0.42	0.48	0.66	0.97	1.11	1.47	0.47	0.48	0.64	0.89	1.06	1.06
	z_c	0.3	0.1	0.1	0.1	0.1	0.1	0.3	0.1	0.1	0.1	0.1	0.1

scale sets the completeness limit in our hydrogen simulation to $M_{\rm H\,I} + M_{\rm H_2} \approx 10^8\ M_\odot$ (Section 3.2; Obreschkow et al. 2009a). Moreover, galaxies with $M_{\rm H\,I} + M_{\rm H_2} \lesssim 10^9\ M_\odot$ normally sit a the centers of dark matter halos with poorly resolved merger histories. Therefore, their properties may not have converged in the semi-analytic simulation (Obreschkow et al. 2009a; Croton et al. 2006).

A long list of limitations associated with the semi-analytic galaxy simulation and our post-processing to assign extended H I and H_2 properties has been considered by Obreschkow et al. (2009a). The bottom line of this discussion is that, at $z \gtrsim 5$, the simulation becomes very uncertain because the geometries and matter content of regular galaxies are virtually unconstrained from an empirical viewpoint. The young age and short merger intervals of these galaxies may, in fact, have caused them to deviate substantially from the simplistic disk-gas model. At $z \lesssim 5$, the predictions of our H I and H_2 properties are more certain, as they are consistent with available observations. For example, two measurements of CO(2–1)-line emission in regular galaxies at $z \approx 1.5$ (Daddi et al. 2008) are consistent with the H_2-MF at this redshift (Obreschkow & Rawlings 2009b). Furthermore, the predicted comoving space density of H_2 evolves proportionally to the observed space density of star formation (e.g., Hopkins 2007) within a factor 2 out to at least $z = 3$. At $z = 0$, the simulated H I-MF and CO(1–0)-luminosity function are consistent with the observations of Zwaan et al. (2005) and Keres et al. (2003). Additionally, the local sizes and line widths of H I and CO match the local observations (Obreschkow et al. 2009a, and references therein).

We shall now highlight some specific limitations associated with the emission lines considered in this paper.

4.2. Limitations Specific to the H I Line

We emphasize that at high redshift, the simulated cosmic H I-space density $\Omega_{\rm H\,I}$ falls below the inferences from Lyα absorption against distant QSOs by a factor ~ 2. As mentioned in Obreschkow & Rawlings (2009b), this could reflect a serious limitations of the semi-analytic models implied by the treatment of all cold hydrogen (H I+H_2) as a single phase. Consequently, our dN/dz predictions for H I could be slightly pessimistic. If we believe the empirical estimations of $\Omega_{\rm H\,I}$, the offset of our H I masses by a factor ~ 2 can be readily accounted for by artificially decreasing the flux limit of the simulated survey by a factor 2. For typical H I surveys in the redshift range $z = 0.5$–10, this would increase the number of detectable sources by a factor 2–4.

We have limited our predictions for H I to H I emission from galaxies. However, in the EoR, the IGM was not completely ionized and therefore acted as an additional source of H I emission or absorption (Iliev et al. 2002). It may therefore be necessary to analyze the implications of intergalactic H I on the detectability of galactic H I at $z \gtrsim 6$ (Becker et al. 2001). On a theoretical level, such an analysis could result from combining the simulation presented in this paper with a simulation of the EoR (e.g., Baek et al. 2009; Santos et al. 2008).

4.3. Limitations Specific to the CO Lines

The main discussion of these limitations is given in Obreschkow & Rawlings (2009b), where we introduced our model for the conversion between H_2 and CO. The most serious sources of uncertainty appear to be the heating of molecular gas by SBs and AGNs, the overlap of molecular clouds at high redshift, and the possible presence of nuclear molecular disks in high-redshift galaxies. By contrast, the often-discussed effects of the CMB and the cosmic evolution of the metallicity seem relatively well understood today. Overall, the uncertainty in the predicted CO luminosities increases with redshift and with the J level of the CO transition.

The highest uncertainties, i.e., those for the higher order CO lines at high redshift, can be close to a factor 10. The dN/dz functions in this regime are therefore expected to deviate significantly from our predictions. Such deviations will uncover much of the physics of CO-line emission. In fact, in Obreschkow & Rawlings (2009b), we have explained in detail how different deviations of the CO-luminosity functions from our predictions can be translated into physical interpretations.

4.4. Is the Simulation Large Enough to Probe Cosmic Structure?

The largest coherence scale of our sky simulation is defined by the size of the periodic simulation box of the underlying dark matter simulation (Millennium Simulation, Springel et al. 2005). The side length of this box is $s_{\rm box} = 500\,h^{-1}$ Mpc, which sets the smallest extractable wave number to $k = 2\pi/s_{\rm box} \approx 0.013\ h$. This value is comparable to the wave number of the first peak in the CDM power spectrum (e.g., Springel et al. 2005). Therefore, the presented simulation allows us to study the power spectrum of H I- and CO-lines and to extract the baryon acoustic oscillations (BAOs); however the position and the amplitude of the first peak of the BAOs will be very poorly constrained.

By contrast, the SKA will have the potential to improve on present measurements of the baryonic power spectrum by at least an order of magnitude in amplitude, and it will detect power in spatial frequencies far below the first acoustic peak. Such a detection could set a primordial constraint on cosmological parameters, especially on the equation of state of dark energy (Blake et al. 2004; Abdalla et al. 2009). Therefore, a simulation of such a detection is regarded as a necessary step in designing the SKA. Yet, this requirement represents a major challenge since no current simulation of cosmic structure is large enough to accurately follow the largest acoustic oscillations, while simultaneously resolving structures small enough to allow the assembly of typical galaxies.

A circumvention of this numerical predicament could result from merging two simulations with different length-scales (see, e.g., Angulo et al. 2008). For example, we could adopt the Horizon-4π dark matter simulation (Prunet et al. 2008; Teyssier et al. 2009), which has a giant box side length of $s_{\rm box} = 2\,h^{-1}$ Gpc, yet 10 times less mass resolution than the Millennium Simulation. Each dark matter halo of the Horizon-4π Simulation could then be populated with the resolved dark matter substructure and the galaxies contained in comparable halos of the Millennium Simulation.

5. CONCLUSION

With this paper, we release a simulation of the H I-emission line and the first 10 $^{12}C^{16}O$-emission lines of galaxies in a sky field with a comoving diameter of $500\,h^{-1}$ Mpc. The actual field of view depends on the (user-defined) maximal redshift $z_{\rm max}$ according to the relation displayed in Figure 2 (see also Equation (5)). This simulation represents the first quantitative attempt to compare the detectability of H I and CO at high redshift. Despite the limitations and uncertainties of this simulation (Section 4), its underlying galaxy simulation is nonetheless consistent with currently available observations (see Obreschkow et al. 2009a; Obreschkow & Rawlings 2009b; Obreschkow et al. 2009b).

While this paper focussed on the simulation techniques and directly accessible results, the list of possible applications of the presented simulation is extensive. Some examples are:

1. a dN/dz analysis for particular surveys with the SKA, the LMT, and ALMA or their pathfinders;
2. a combined study of H I emission from galaxies and H I emission from the IGM during the EoR (Santos et al. 2008) to quantify confusion issues;
3. an optimization of the survey time allocated to different ALMA bands based on the CO-line ratios predicted at various redshifts;
4. first quantitative predictions of the SKA's and ALMA's abilities to probe the galaxy power spectrum;
5. predictions of the absorption signatures of H I and CO against distant QSOs;
6. a study of line stacking experiments at redshifts where the detection of individual galaxies becomes impossible.

Such predictions can assist the design and optimized use of telescopes, such as the LMT, the SKA, ALMA, and their pathfinders. Moreover, in light of forthcoming observations with those future instruments, the predictions made *prior* to these observations are the safest and perhaps the only way to test the predictive power of our current theories. This feature accentuates the necessity of extensive predictions, whether they will be verified or not by the empirical data.

This effort/activity is supported by the European Community Framework Programme 6, Square Kilometre Array Design Studies (SKADS), contract No. 011938. The Millennium Simulation databases and the web application providing online access to them were constructed as part of the activities of the German Astrophysical Virtual Observatory.

APPENDIX A

HOW TO RECOVER LINE PROFILES FROM CATALOG PROPERTIES

In Section 2.4, the normalized profiles of the H I- and CO-emission lines have been parameterized using the five parameters $\Psi_0^{\rm obs}$, $\Psi_{\rm max}^{\rm obs}$, $w_{\rm peak}^{\rm obs}$, $w_{50}^{\rm obs}$, and $w_{20}^{\rm obs}$ (see Figure 8). From these parameters, the original normalized velocity profiles $\Psi(V)$ can be approximately recovered using the analytic function

$$\Psi_{\rm approx}(V) = \begin{cases} k_3 \exp\left[-\frac{(|V|-k_1)^2}{k_2}\right] & \text{if} |V| \geqslant w_{\rm peak}^{\rm obs}/2, \\ \frac{k_5}{\sqrt{k_4 - V^2}} & \text{if} |V| < w_{\rm peak}^{\rm obs}/2, \end{cases} \tag{A1}$$

where k_i, $i \in \{1, \ldots, 5\}$, are free parameters. Equation (A1) combines the functional form of Equation (42) in Obreschkow et al. (2009a) for the center of the emission line with a Gaussian for the tails of the emission line. The five parameters k_i can be inferred from the parameters $\Psi_0^{\rm obs}$, $\Psi_{\rm max}^{\rm obs}$, $w_{\rm peak}^{\rm obs}$, $w_{50}^{\rm obs}$, and $w_{20}^{\rm obs}$. The analytic solution is

$$k_1 = \frac{1}{4} \frac{\ln(0.5)\left({w_{\rm peak}^{\rm obs}}^2 - {w_{20}^{\rm obs}}^2\right) + \ln(0.2)\left({w_{50}^{\rm obs}}^2 - {w_{\rm peak}^{\rm obs}}^2\right)}{\ln(0.5)\left(w_{\rm peak}^{\rm obs} - w_{20}^{\rm obs}\right) + \ln(0.2)\left(w_{50}^{\rm obs} - w_{\rm peak}^{\rm obs}\right)}, \tag{A2}$$

$$k_2 = \frac{0.25\left({w_{\rm peak}^{\rm obs}}^2 - {w_{50}^{\rm obs}}^2\right) + k_1\left(w_{50}^{\rm obs} - w_{\rm peak}^{\rm obs}\right)}{\ln(0.5)}, \tag{A3}$$

$$k_3 = \Psi_{\rm max}^{\rm obs} \exp\left[\frac{\left(2k_1 - w_{\rm peak}^{\rm obs}\right)^2}{4k_2}\right], \tag{A4}$$

$$k_4 = \frac{1}{4} \frac{{w_{\rm peak}^{\rm obs}}^2 {\Psi_{\rm max}^{\rm obs}}^2}{{\Psi_{\rm max}^{\rm obs}}^2 - {\Psi_0^{\rm obs}}^2}, \tag{A5}$$

$$k_5 = \Psi_0^{\rm obs}\sqrt{k_4}. \tag{A6}$$

Figure 8 compares a simulated normalized H I-emission line with the emission line recovered using Equations (A1)–(A6).

We note that some emission lines, especially those of galaxies seen face-on, peak at the line center. These lines have $w_{\rm peak}^{\rm obs} = 0$, and therefore Equation (A1) reduces to the Gaussian tails.

APPENDIX B

ONLINE-ACCESS TO THE SKY SIMULATION

One particular realization of the mock observing cone, i.e., one choice of random symmetry operations for the replicated simulation boxes (see Section 2.2), can be access online via http://s-cubed.physics.ox.ac.uk/ (go to "S^3-SAX-Sky"). Each galaxy in the virtual observing cone is specified by a list of properties, including its position, its attributes for the H I- and CO-emission lines, as well as its intrinsic properties of the DeLucia-catalog, such as optical magnitudes, masses, star formation rates, clustering properties, or merger histories.

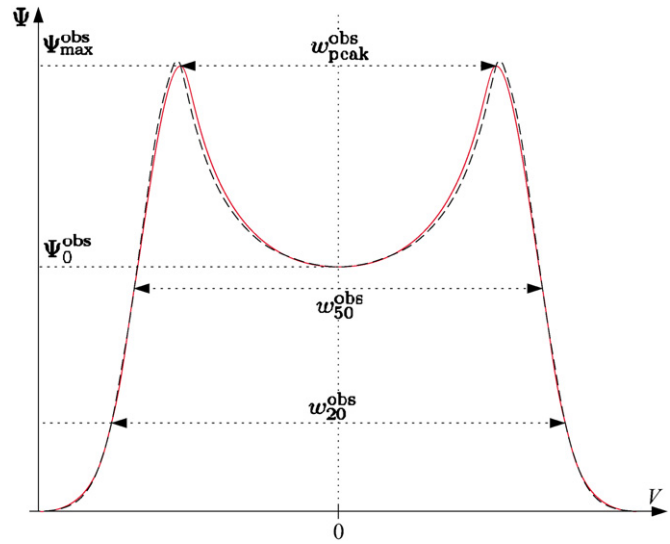

Figure 8. Comparison of a simulated normalized emission line $\Psi(V)$ (solid line) with the emission line $\Psi_{\rm approx}(V)$ (dashed line), recovered from the five parameters $\Psi_0^{\rm obs}$, $\Psi_{\rm max}^{\rm obs}$, $w_{\rm peak}^{\rm obs}$, $w_{50}^{\rm obs}$, and $w_{20}^{\rm obs}$.
(A color version of this figure is available in the online journal.)

The accessible database contains two subsets, a full sky simulation ($\sim 2.8 \times 10^8$ galaxies), associated with the Millennium Simulation ($s_{\rm box} = 500\,h^{-1}$ Mpc), and a small sky simulation ($\sim 4.5 \times 10^6$ galaxies), associated with the Milli-Millennium Simulation ($s_{\rm box} = 62.5\,h^{-1}$ Mpc). The solid angle subtended by the small sky simulation is 64 times smaller than of the full sky simulation. However, the small simulation can be useful for testing purposes, since it can be accessed and post-processed 10–100 times faster.

The maximal opening angle φ of the sky field depends on the maximal comoving distance $D_{\rm C,max}$ (or the maximal redshift $z_{\rm max}$) via Equation (5) (see also Figure 2). The user must be aware that there are no galaxies outside this maximal opening angle, i.e., galaxies only exist, where |R.A.| and |decl.| are smaller than $\varphi/2$.

The database can be queried using the structured query language (SQL) interface. The latter not only allows the user to download a particular galaxy sample, but it also offers ways to directly calculate dN/dz functions and luminosity functions or to retrieve all the galaxies of a particular cluster. Samples of such advanced queries are given on the web-page.

APPENDIX C

ILLUSTRATION OF A SKY FIELD IN DIFFERENT REDSHIFT BINS

Figure 9 shows the H I and CO of the galaxies in a mock sky field of 3×1 arcmin^2 at three different redshifts. Each redshift slice has the same comoving thickness of 240 Mpc, such that the number of galaxies is proportional to the comoving space density of galaxies. Note, however, that the flux scales differ between the three panels of Figure 9. The main features of the galaxies in Figure 9 are discussed in Section 3.1.

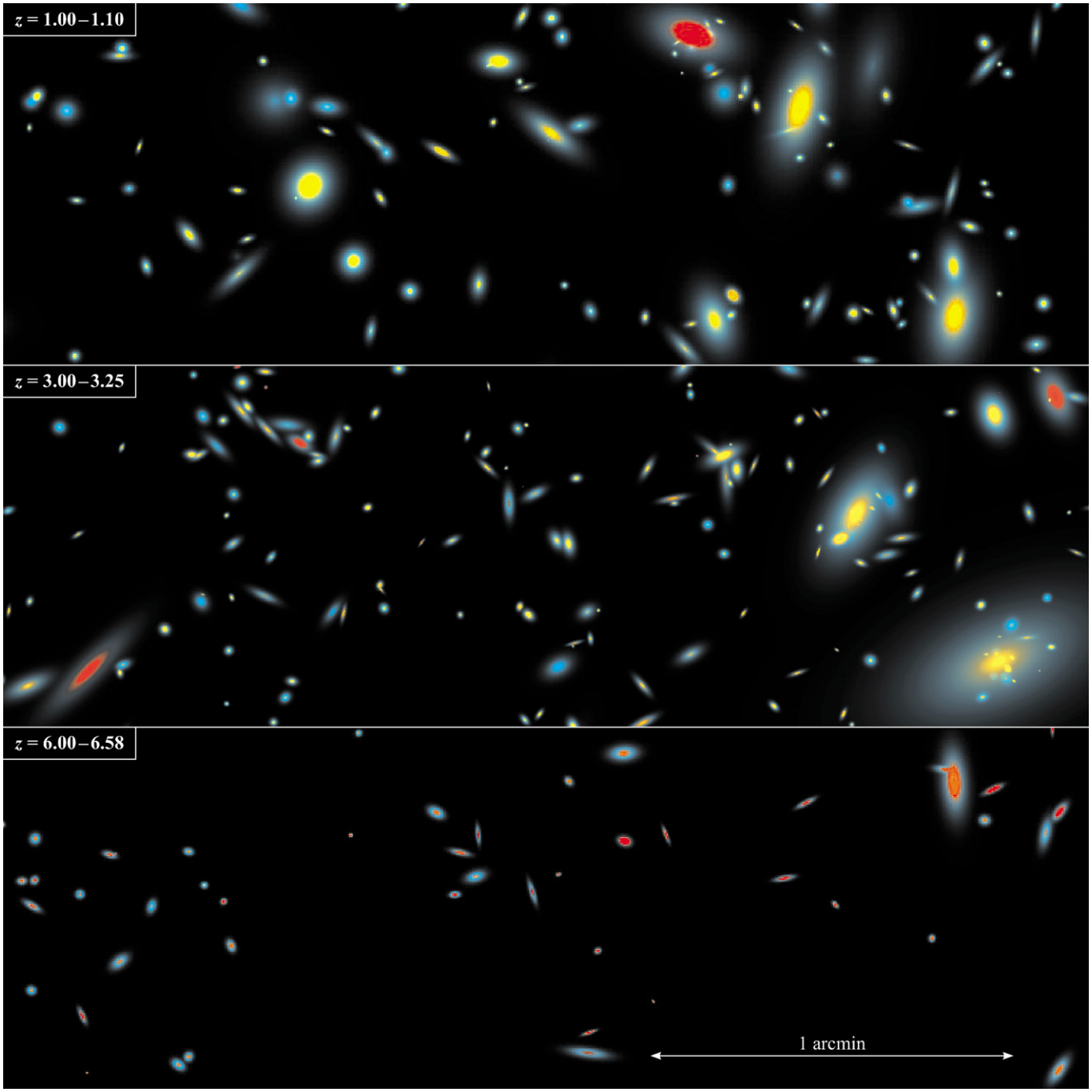

Figure 9. Simulated sky field covering 3×1 arcmin^2. The three panels correspond to three different redshift slices, with an identical comoving depth of 240 Mpc. The coloring is identical to Figure 4, but the flux scales are 10 times smaller at $z = 3$ and 100 times smaller at $z = 6$.

APPENDIX D

ANALYTIC FITS FOR dN/dz-FUNCTIONS

Table 1 lists the values of the parameters c_1, c_2, and c_3 for the analytic dN/dz fit of Equation (15). The parameters are given for both peak-flux-density-limited and integrated-flux-limited surveys, although the functions have only been displayed for the peak flux density limited case. Since apparent line widths are typically of order 100 km s^{-1}, surveys limited by a flux density $s_{\rm lim}$ and those limited by a velocity-integrated flux $S^{\rm V}_{\rm lim} = s_{\rm lim} \times 100$ km s^{-1} have similar dN/dz functions.

The sensitivity of a survey may be high enough that galaxies are detected in regions of the galaxy MF, where the simulation is incomplete. In fact, for each emission line and each sensitivity limit, there is a critical redshift $z_{\rm c}$, below which sources of the incomplete part of the simulated galaxy MF will be detected at a sufficiently high rate that the number of real detections will significantly exceed the number of simulated detections. Therefore, the simulated dN/dz functions at $z \leqslant z_{\rm c}$ must be considered as lower limits. As in Section 3.2, we shall define $z_{\rm c}$ as the redshift, below which the fraction of sources with hydrogen masses below 10^8 $M_\odot$ (completeness limit) is larger than 1%, noting that the fraction of actually

missing sources may be much larger due to incompleteness (see Section 3.2).

REFERENCES

Abdalla, F., Blake, C., & Rawlings, S. 2009, MNRAS, submitted (arXiv:0905.4311)
Abdalla, F. B., & Rawlings, S. 2005, MNRAS, 360, 27
Angulo, R. E., Baugh, C. M., Frenk, C. S., & Lacey, C. G. 2008, MNRAS, 383, 755
Baek, S., di Matteo, P., Semelin, B., Combes, F., & Revaz, Y. 2009, A&A, 495, 389
Becker, R. H., et al. 2001, AJ, 122, 2850
Binney, J., & Merrifield, M. 1998, Galactic Astronomy (Princeton, NJ: Princeton Univ. Press)
Blain, A. W., Frayer, D. T., Bock, J. J., & Scoville, N. Z. 2000, MNRAS, 313, 559
Blaizot, J., Wadadekar, Y., Guiderdoni, B., Colombi, S. T., Bertin, E., Bouchet, F. R., Devriendt, J. E. G., & Hatton, S. 2005, MNRAS, 360, 159
Blake, C. A., Abdalla, F. B., Bridle, S. L., & Rawlings, S. 2004, New Astron. Rev., 48, 1063
Blitz, L., & Rosolowsky, E. 2006, ApJ, 650, 933
Boomsma, R., van der Hulst, J. M., Oosterloo, T. A., & Sancisi, R. 2002, BAAS, 34, 708
Braine, J., Combes, F., Casoli, F., Dupraz, C., Gerin, M., Klein, U., Wielebinski, R., & Brouillet, N. 1993, A&AS, 97, 887
Carilli, C. L., & Blain, A. W. 2002, ApJ, 569, 605
Carilli, C. L., & Rawlings, S. 2004, New Astron. Rev., 48, 979
Catinella, B., Haynes, M. P., Giovanelli, R., Gardner, J. P., & Connolly, A. J. 2008, ApJ, 685, L13
Cole, S., et al. 2001, MNRAS, 326, 255
Combes, F., Maoli, R., & Omont, A. 1999, A&A, 345, 369
Croton, D. J., et al. 2006, MNRAS, 365, 11
Daddi, E., Dannerbauer, H., Elbaz, D., Dickinson, M., Morrison, G., Stern, D., & Ravindranath, S. 2008, ApJ, 673, L21
De Lucia, G., & Blaizot, J. 2007, MNRAS, 375, 2
Ferrière, K. M. 2001, Rev. Mod. Phys., 73, 1031
Förster Schreiber, N. M., et al. 2006, ApJ, 645, 1062
Genzel, R., et al. 2008, ApJ, 687, 59
Giovanelli, R., Haynes, M. P., da Costa, L. N., Freudling, W., Salzer, J. J., & Wegner, G. 1997, ApJ, 477, L1
Greve, T. R., Papadopoulos, P. P., Gao, Y., & Radford, S. J. E. 2009, ApJ, 692, 1432
Greve, T. R., & Sommer-Larsen, J. 2008, A&A, 480, 335
Gunn, J. E., & Gott, J. R. I. 1972, ApJ, 176, 1
Häring, N., & Rix, H.-W. 2004, ApJ, 604, L89
Hopkins, A. M. 2007, in ASP Conf. Ser. 380, Deepest Astronomical Surveys, ed. J. Afonso, H. C. Ferguson, B. Mobasher, & R. Norris (San Francisco, CA: ASP), 423
Huang, J.-S., Glazebrook, K., Cowie, L. L., & Tinney, C. 2003, ApJ, 584, 203
Iliev, I. T., Shapiro, P. R., Ferrara, A., & Martel, H. 2002, ApJ, 572, L123
Kannappan, S. J., Fabricant, D. G., & Franx, M. 2002, AJ, 123, 2358
Keres, D., Yun, M. S., & Young, J. S. 2003, ApJ, 582, 659
Kregel, M., van der Kruit, P. C., & de Grijs, R. 2002, MNRAS, 334, 646
Lah, P., et al. 2007, MNRAS, 376, 1357
Leroy, A. K., Walter, F., Brinks, E., Bigiel, F., de Blok, W. J. G., Madore, B., & Thornley, M. D. 2008, AJ, 136, 2782
Meyer, M. J., et al. 2004, MNRAS, 350, 1195
Norberg, P., et al. 2002, MNRAS, 336, 907
Noterdaeme, P., Ledoux, C., Petitjean, P., & Srianand, R. 2008, A&A, 481, 327
Obreschkow, D., Croton, D., DeLucia, G., Khochfar, S., & Rawlings, S. 2009a, ApJ, 698, 1467
Obreschkow, D., & Rawlings, S. 2009a, ApJ, 698, 1467
Obreschkow, D., & Rawlings, S. 2009b, ApJ, 696, L129
Obreschkow, D., Rawlings, S., Heywood, I., & Klöckner, H.-R. 2009b, ApJ, 702, 1321
Papadopoulos, P. P., Röttgering, H. J. A., van der Werf, P. P., Guilloteau, S., Omont, A., van Breugel, W. J. M., & Tilanus, R. P. J. 2000, ApJ, 528, 626
Prochaska, J. X., Herbert-Fort, S., & Wolfe, A. M. 2005, ApJ, 635, 123
Prunet, S., Pichon, C., Aubert, D., Pogosyan, D., Teyssier, R., & Gottloeber, S. 2008, ApJS, 178, 179
Richmond, M. W., & Knapp, G. R. 1986, AJ, 91, 517
Rupen, M. P. 1991, AJ, 102, 48
Santos, M. G., Amblard, A., Pritchard, J., Trac, H., Cen, R., & Cooray, A. 2008, ApJ, 689, 1
Springel, V., et al. 2005, Nature, 435, 629
Tacconi, L. J., et al. 2006, ApJ, 640, 228
Teyssier, R., et al. 2009, A&A, 497, 335
Tremonti, C. A., et al. 2004, ApJ, 613, 898
Verheijen, M., van Gorkom, J. H., Szomoru, A., Dwarakanath, K. S., Poggianti, B. M., & Schiminovich, D. 2007, ApJ, 668, L9
Wall, W. F. 2006, Rev. Mex. Astron. Astrofis., 42, 117
Walter, F., Carilli, C., Bertoldi, F., Menten, K., Cox, P., Lo, K. Y., Fan, X., & Strauss, M. A. 2004, ApJ, 615, L17
Wang, J., De Lucia, G., Kitzbichler, M. G., & White, S. D. M. 2008, MNRAS, 384, 1301
Weiss, A., Downes, D., Neri, R., Walter, F., Henkel, C., Wilner, D. J., Wagg, J., & Wiklind, T. 2007, A&A, 467, 955
Wilman, R. J., et al. 2008, MNRAS, 388, 1335
Young, L. M. 2002, AJ, 124, 788
Zwaan, M. A., Meyer, M. J., Staveley-Smith, L., & Webster, R. L. 2005, MNRAS, 359, L30